A 100-MESFET Planar Grid Oscillator

Zoya B. Popović, Robert M. Weikle II, Moonil Kim, and David B. Rutledge, *Senior Member, IEEE*

Abstract—**In this work we present a 100-MESFET oscillator which gives 21 W of CW effective radiated power (ERP) with a 16 dB directivity and a 20% dc to RF conversion efficiency at 5 GHz. The oscillator is a planar grid structure periodically loaded with transistors. The grid radiates and the devices combine quasi-optically and lock to each other. The oscillator can also be quasi-optically injection-locked to an external signal. The planar grid structure is very simple. All of the devices share the same bias, and they can be power and frequency tuned with a mirror behind the grid or dielectric slabs in front of it. An equivalent circuit for an infinite grid predicts the mirror frequency tuning. The planar property of the oscillator offers the possibility of a wafer-scale monolithically integrated source. Thousands of active solid-state devices can potentially be integrated in a high-power source for microwave or millimeter-wave applications.**

I. Introduction

In the microwave and millimeter-wave regions solid-state oscillators have limited output power levels. However, the alternative high-power sources are tubes, which are bulky, very expensive, have a limited lifetime, and require high-voltage power supplies. Combining a large number of low-power, solid-state devices becomes attractive. Mink [1] proposed a power-combining scheme where a grid loaded with devices is placed in a quasi-optical resonator. Recently, MESFET [2], [3] and Gunn-diode [4] quasi-optical power-combining oscillators have been presented with effective radiated powers (ERP's) as high as 37 W [2]. However, these oscillators are three-dimensional structures not suitable for monolithic wafer-scale integration. In addition, the Gunn-diode array requires a separate bias supply for each diode.

In the meantime, solid-state technology has continued to improve. Recent efforts in HEMT devices [5] have resulted in a 23% power-added efficiency at 93 GHz with an output power of 18 mW. HBT's [6] have promising high-power applications with good yields and power-added efficiencies of 40% at 12 GHz with output powers of 10 W. Quantum-well devices have pushed the frequency limit to 420 GHz [7] with an output power of 200 nW. These advances in device technology make wafer-scale integrated power-combining sources very attractive. It should be possible to manufacture the grid oscillator presented here as a planar monolithic circuit which can combine a very large number of two- or three-terminal devices. This approach could give very high power solid-state oscillators in the 30–40 GHz range and reasonable power levels from low-power devices above 100 GHz. The grid oscillator is an antenna as well as a source. High directivity and a high ERP can be achieved at millimeter-wave frequencies, where a 2 in. wafer is many wavelengths across.

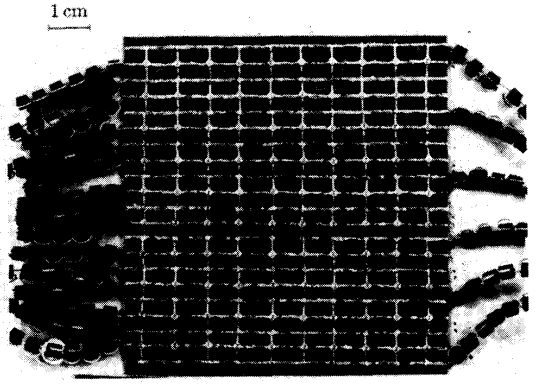

Fig. 1. The 100-MESFET planar grid oscillator. The horizontal lines are the bias lines. Ferrite beads are added to the bias lines to suppress low-frequency oscillations. All the gates, drains, and sources are connected, so there are a total of three wires used for the grid bias. The vertical leads are gates and drains and the radiated electric field is polarized in this direction.

The planar grid oscillator is shown in Fig. 1. The transistors are Fujitsu GaAs MESFET's (FSC11LF), made for satellite receivers at 4 GHz, which typically produce 20 mW in a microstrip oscillator. The devices in adjacent rows share the gate and drain bias lines. The symmetry of the grid forces cancellation of RF currents along the horizontal bias lines, so that the radiation is primarily from the vertical drain and gate leads. The grid is made on a 0.5-mm-thick, low-dielectric-constant ($\epsilon_r = 2.2$) material on top of a 2.5-mm-thick Duroid slab with $\epsilon_r = 10.5$. There is a flat metal mirror behind the grid. The mirror and the grid form a Fabry–Perot cavity about a wavelength long. When the bias to the transistors is turned on, oscillations build up, and all the cavity modes compete. The mode with the lowest diffraction loss per round-trip survives, and the devices in the grid lock to this mode. This grid locks at 5 GHz. Fig. 2 shows the measured pattern with the mirror 57 mm away from the back of the substrate. The ERP is 22 W, and the directivity is 16 dB. The RF to dc efficiency is 20%, and the isotropic conversion gain [8] is 8.5 dB. The cross-polarized component is 30 dB below the copolar one at the pattern peak.

Manuscript received April 26, 1990; revised October 25, 1990. This work was supported by the Army Research Office and the Northrop Corporation.

Z. B. Popović was with the Division of Engineering and Applied Sciences, California Institute of Technology, Pasadena. She is now with the Department of Electrical and Computer Engineering, University of Colorado, Boulder, CO 80309.

R. M. Weikle II, M. Kim, and D. B. Rutledge are with the Division of Engineering and Applied Sciences, California Institute of Technology, Pasadena, CA 91125.

IEEE Log Number 9041468.

0018-9480/91/0200-0193$01.00 ©1991 IEEE

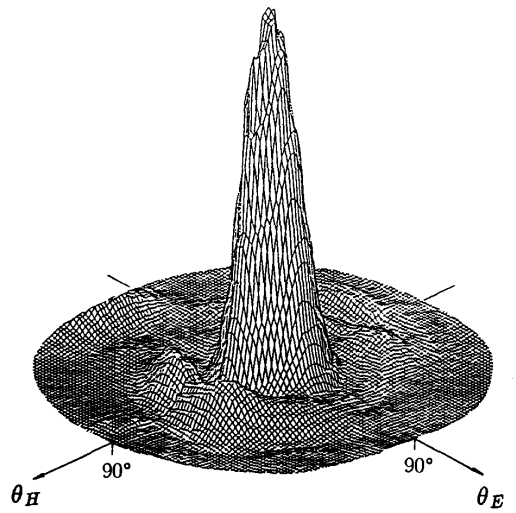

Fig. 2. The measured radiation pattern of the grid. The vertical scale is linear in power. The axes are given in terms of spherical coordinates by $\theta_E = \theta \sin\phi$ and $\theta_H = \theta \cos\phi$.

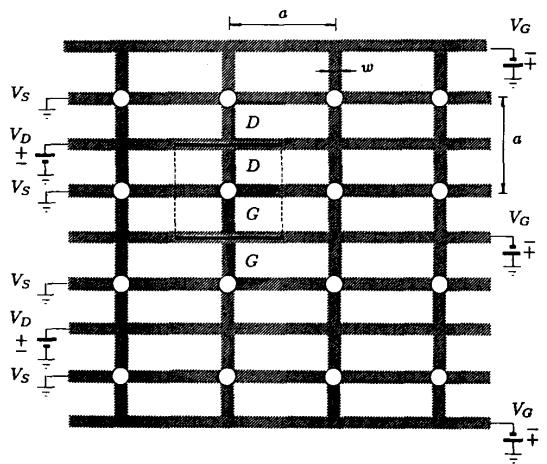

Fig. 3. Boundary conditions are imposed by the grid symmetry. The solid lines are electric walls ($E_{\text{tangential}} = 0$) and the dashed lines are magnetic walls ($H_{\text{tangential}} = 0$). In the actual grid $a = 8$ mm and $w = 1$ mm.

II. Equivalent Circuit

In an infinite grid with all the devices locked in phase, symmetry allows us to represent the grid as an equivalent waveguide unit cell. This waveguide has magnetic walls on the sides and electric walls on the top and bottom, as shown in Fig. 3. It extends to the $+z$ and $-z$ directions, with the grid in the $z = 0$ plane. The propagating mode is TEM. The evanescent modes present reactances at the device terminals. These reactances are found by the EMF method [9]. This simple approach is justified by the fact that the period is only $\lambda/8$. The reactances depend on the electrical thickness of the dielectric which supports the grid, on the geometry of the

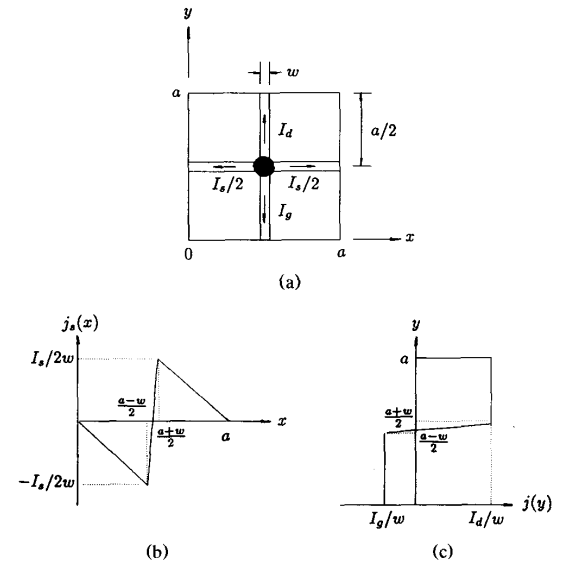

Fig. 4. (a) Transistor in unit waveguide with (b) source and (c) drain and gate current distributions. The gate and drain currents are different. The current distribution inside the device is assumed to be linear to avoid discontinuities.

grid, and on the assumed current distribution on the transistor leads, shown in Fig. 4. The results presented here are derived from a first-order assumption for the currents: a uniform current in the gate and drain leads, and a linear current in the source lead. The latter is set to zero at the magnetic walls to satisfy the boundary conditions.

The embedding circuit for a device in the grid is shown in Fig. 5. The inductors in the gate and the drain are the lead inductances. The derivations of the expressions for the circuit elements are somewhat lengthy, but they essentially follow the procedure in Eisenhart and Kahn's paper for a post in a waveguide [10]. The circuit elements obtained in this way are given by

$$L = \frac{1}{j\omega} \sum_{\substack{m=2 \\ m \text{ even}}}^{\infty} \operatorname{sinc}^2\left(\frac{m\pi w}{2a}\right) Z_{m0}^{\text{TE}} \tag{1}$$

$$L_S = \frac{1}{j\omega}\left(\frac{2}{a}\right)^2 \sum_{\substack{n \text{ odd} \\ m \text{ even}}} \frac{1}{k_{mn}^2} \operatorname{sinc}^2\left(\frac{n\pi w}{2a}\right) \times \operatorname{sinc}^2\left(\frac{m\pi w}{2a}\right)\left(\frac{m}{n} + \frac{n}{m}\frac{a}{a-w}\right)^2 Z_{mn}^{\text{TE}} \tag{2}$$

$$C_S^{-1} = j\omega\left(\frac{2}{a}\right)^2 \left[\sum_{\substack{n=1 \\ n \text{ odd}}}^{\infty} \frac{1}{2k_{0n}^2} \operatorname{sinc}^2\left(\frac{n\pi w}{2a}\right) Z_{0n}^{\text{TM}} + 2 \sum_{\substack{n \text{ odd} \\ m \text{ even}}} \frac{1}{k_{mn}^2} \operatorname{sinc}^2\left(\frac{n\pi w}{2a}\right) \cdot \operatorname{sinc}^2\left(\frac{m\pi w}{2a}\right)\left(1 - \frac{a}{a-w}\right)^2 Z_{mn}^{\text{TM}} \right] \tag{3}$$

where $k_{mn}^2 = (2\pi/\lambda)^2 - (m\pi/2a)^2 - (n\pi/2a)^2$, and Z_{mn}^{TE}

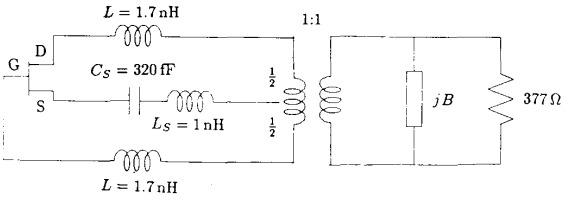

Fig. 5. The equivalent circuit for the grid at 5 GHz.

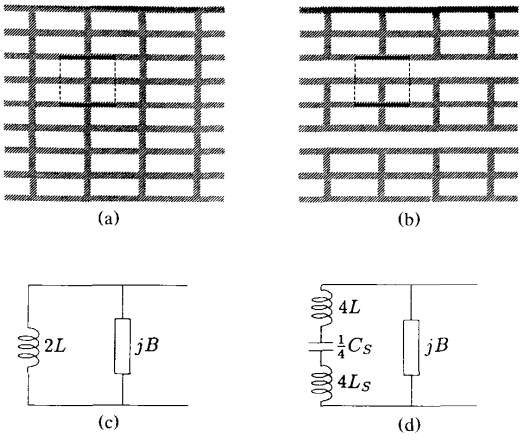

Fig. 6. (a) Inductive and (b) capacitive grids. The dimensions of the unit cell are the same as for the MESFET grid. Equivalent circuits for the (c) inductive and (d) capacitive grids.

and Z_{mn}^{TM} are the impedances of the mn-th TE and TM modes [9]. Each of these is a parallel combination of the impedances in the $+z$ and $-z$ directions. Free space is represented as a 377Ω transmission line, and the mirror is represented as a shunt reactance jB.

The entire grid is in this way reduced to a one-port equivalent. The measured small-signal transistor s parameters were used, and the saturation is taken into account by reducing $|s_{21}|$. The impedance looking into the oscillator from the 377 Ω load was examined as a function of frequency. When this impedance becomes -377 Ω, an oscillation should occur.

We tested the equivalent circuit by building two grids with the same dimensions but with shorting strips instead of transistors, as shown in parts (a) and (b) of Fig. 6. The substrates are Rogers Duroid, 2.5 mm thick and 10 cm square, with a nominal dielectric constant of 10.5 and copper cladding on the back. The equivalent circuits for these two grids, shown in parts (c) and (d), use the same formulas for the inductances and capacitance as the transistor grid. The phase of the reflection coefficient of the grid was measured from 2 to 18 GHz in an anechoic chamber with a wide-band horn and an HP 8510 network analyzer. The calibration was quasi-optical. A microwave absorber at a 45° angle served as the matched load, and a copper sheet as the short. The copper sheet was translated to provide a delayed short as the third standard. The reflection coefficient phases are shown in Fig. 7. The theoretical phase calculated from the equivalent models is shown in solid line for comparison. The

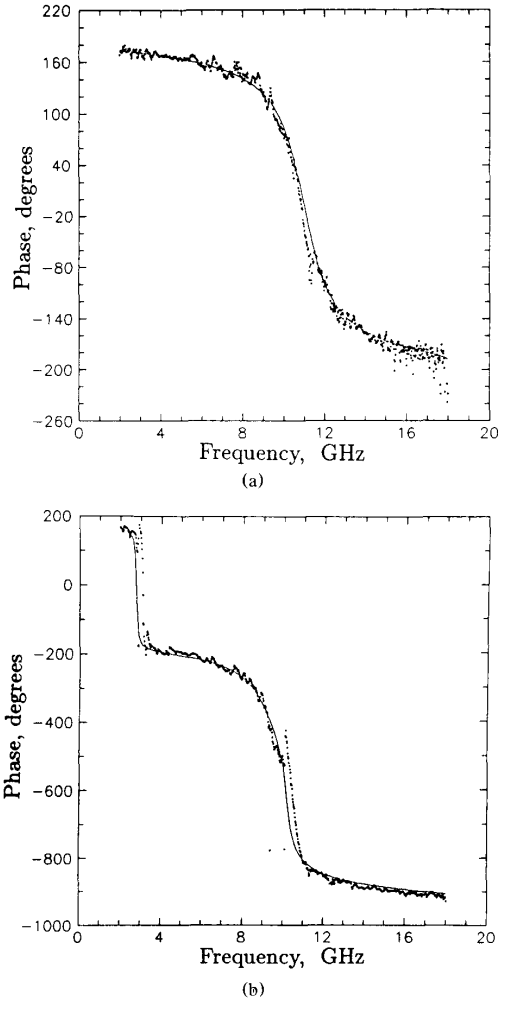

Fig. 7. Measured (dots) and theoretical (solid line) phase of the reflection coefficient for the (a) inductive grid and (b) capacitive grid. Note that the two phase scales are quite different.

substrate electrical thickness which is used in the model was measured by stripping the grid pattern and repeating the reflection phase measurement. The close agreement between theory and experiment gives us confidence in the equivalent circuit model.

III. Tuning Measurements

The position of the mirror has a strong effect on the frequency of oscillation, the grid output power, and the radiation pattern (Figs. 8 and 9). The equivalent circuit in Fig. 5 predicts frequency tuning as a function of the mirror position. In this simple transmission-line model, the oscillation frequency does not change if the mirror spacing is increased by $\lambda/2$, as shown in the solid lines in Fig. 8(a). The experimental results, shown with dots, agree with the theory. The mirror position affects the width of the main lobe and the size of the side lobes, as shown in Fig. 9. The

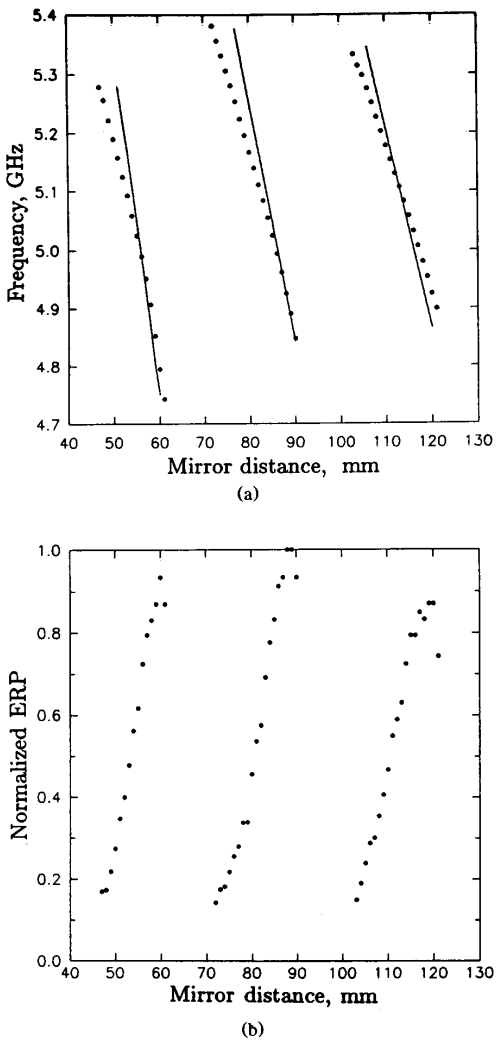

Fig. 8. The theoretical (solid line) and measured (dots) frequency tuning with (a) mirror position. (b) Measured power tuning.

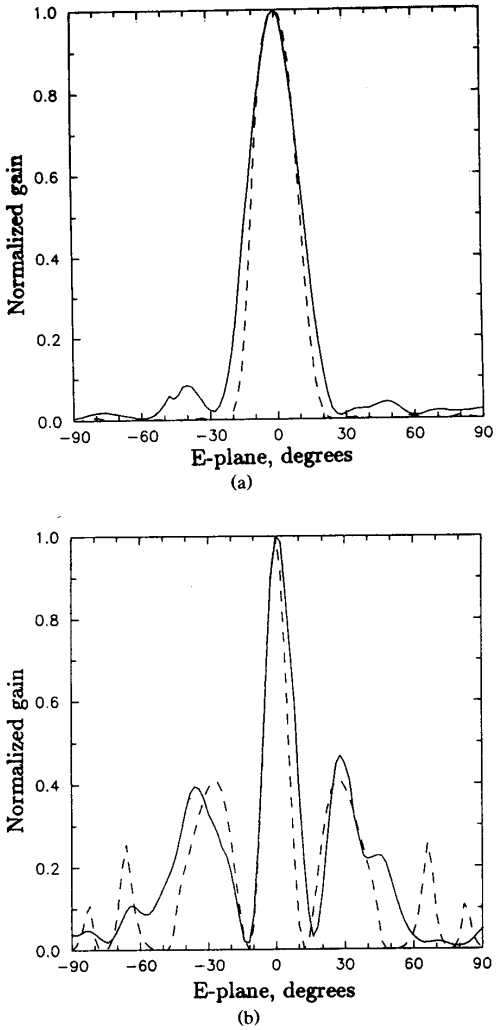

Fig. 9. Experimental pattern (solid line) for a mirror distance of (a) 54 mm and (b) 82 mm. Theoretical pattern (dashed line) for a mirror distance of (a) 62 mm and (b) 88 mm.

theoretical pattern of the grid is calculated for a uniform array of short dipoles on an infinite dielectric, with an infinite mirror in the back [11]. The distances at which the theory predicts similar patterns are several millimeters larger than seen in the experiment.

IV. Injection Locking

In the measured results presented so far, the MESFET's were locked together with no external locking signal present. For some applications it is convenient to be able to lock the devices to an externally injected signal. For example, an electrically modulated low-power oscillator can frequency modulate the source. The injected signal can also stabilize the frequency, as shown in Fig. 10. The injection locking was performed quasi-optically, as shown in Fig. 11. The measured injection-locking bandwidth as a function of the injected power is shown in Fig. 12. It is proportional to the square root of the injected power or, equivalently, to the injected field magnitude, as expected [12].

Previous injection-locking analysis [12] has been based on the assumption that the device impedance is a function of power only, and the load impedance is a function of frequency. For the grid, the impedance is a function of both power and frequency, while the load, which is free space, is independent of power and frequency. This suggests a different approach. We use the equivalent circuit shown in Fig. 13(a). The grid is represented by a reflection coefficient $s_g(p, f)$, which is a function of the transmitted power, p, and the frequency, f. Free space is represented by a load with a reflection coefficient of zero. The radiated signal is represented by a wave amplitude a, where the magnitude of a is the square root of the radiated power. The injected signal is

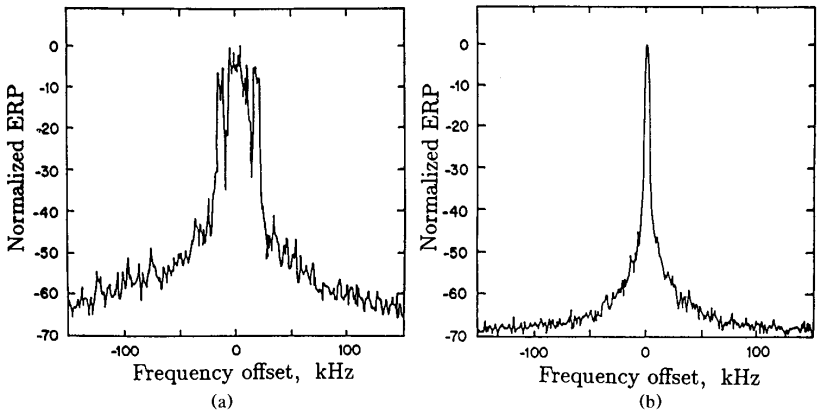

Fig. 10. The (a) free-running and (b) injection-locked grid spectra. The center frequency is 5.2 GHz.

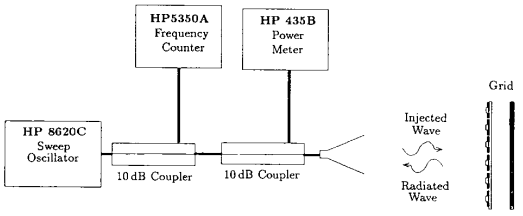

Fig. 11. Quasi-optical injection-locking measurement setup.

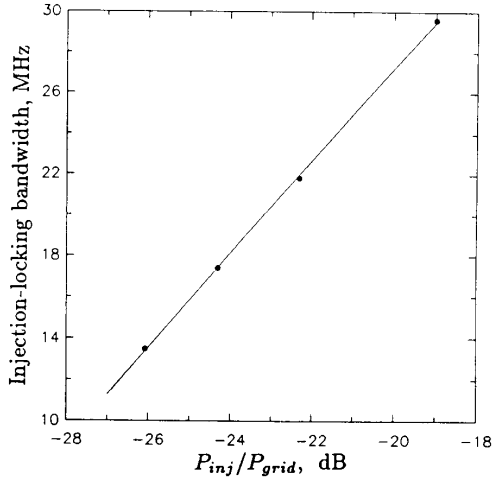

Fig. 12. The dependence of the grid locking range on the power ratio of the injected and free-running signal for a mirror distance of 55 mm.

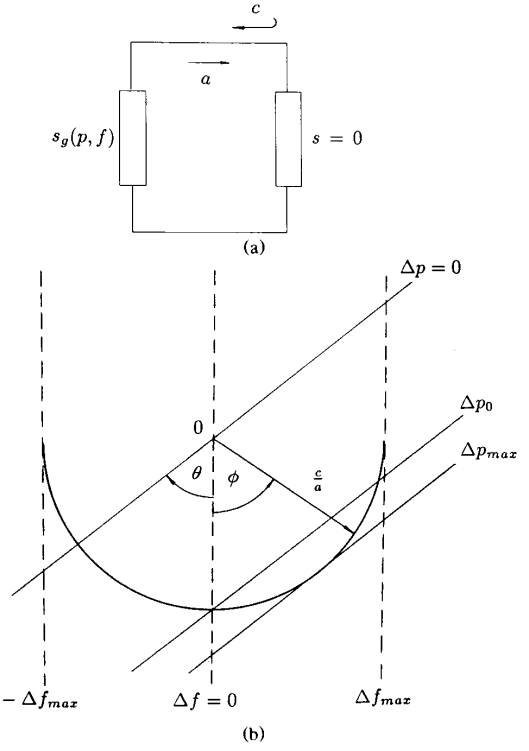

Fig. 13. (a) The equivalent circuit of the injection-locked grid oscillator, where a is the wave radiated from the grid and c is the injected signal wave. The reflection coefficient of the grid $s_g(p,f)$ is a function of both power and frequency. (b) Contours of constant Δp and Δf in the $1/s_g$ complex plane.

written as c, where the magnitude of c is the square root of the injected power. From the circuit model we can write the relation

$$s_g(p,f) = a/c. \tag{4}$$

Fig. 13(b) is a Rieke diagram showing $1/s_g$ in the complex plane. This is a convenient representation because the origin represents the free-running oscillation condition. The contours of constant power and frequency may be drawn as straight lines in a small neighborhood about the origin. As the frequency varies, the tip of the c/a arrow will trace out a semicircle, provided that the injected power remains the same and the deviation in the radiated power is small. The

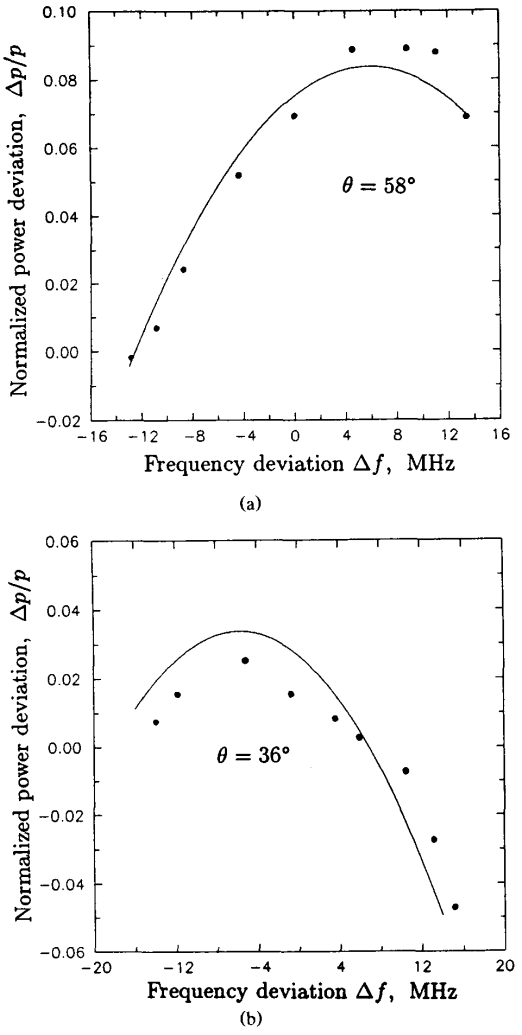

Fig. 14. Variation of the oscillator output power inside the locking range for two different mirror positions. (a) 89 mm and (b) 82 mm. The solid lines are calculated from measured values of Δf_{max}, Δp_{max}, and Δp_0.

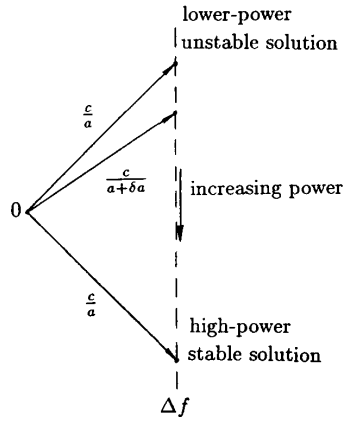

Fig. 15. Stability in injection locking. There are two solutions, but only the higher power one is stable.

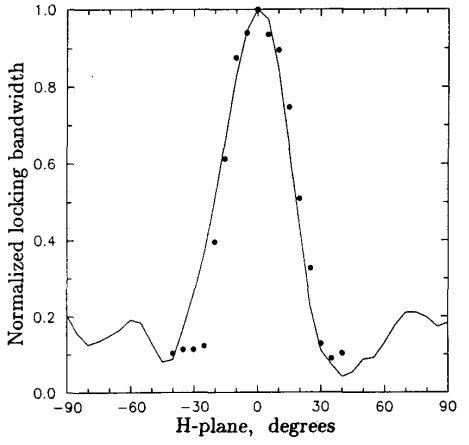

Fig. 16. Normalized injection-locking bandwidth (dots) measured as the incident angle of the injected signal varies in the H plane. At larger angles the injected signal power is not sufficient to lock the grid. The solid line shows the measured free-running far-field H-plane pattern. These two curves are effectively the grid receiving and transmitting patterns, and they are closely related by reciprocity.

frequency deviation varies symmetrically around the free-running frequency from $-\Delta f_{max}$ to $+\Delta f_{max}$, where $2\Delta f_{max}$ is the injection-locking bandwidth. The power deviation, Δp, inside the locking range is not symmetrical in general. From Fig. 13(b), the frequency and power of an injection locked-oscillator are given by

$$\Delta f = \Delta f_{max} \sin \phi \tag{5}$$

$$\Delta p = \Delta p_{max} \sin(\phi + \theta) \tag{6}$$

$$\theta = \arcsin(\Delta p_0 / \Delta p_{max}) \tag{7}$$

where θ is the angle between the contours of constant Δf and Δp, and ϕ changes from $-\pi/2$ to $+\pi+2$ inside the locking range. The quantity Δp_0 is the change in oscillator power at the free-running frequency after locking. This means that it is sufficient to measure Δf_{max}, Δp_{max}, and Δp_0 in order to predict the injection-locked oscillator behavior. Fig. 14 shows measured and calculated power variation of the injection-locked grid for two different mirror positions.

For a given frequency and injected signal level, there are actually two possible solutions (Fig. 15). However, only the higher power solution is stable, and this is what makes the c/a locus in Fig. 13(b) a semicircle rather than a full circle. We can understand this by considering a perturbation δa from the unstable solution. We will assume that δa increases the transmitted power, so that the tip of the c/a arrow moves down the Δf contour. However, this increases the power further, so that the arrow does not stop until it reaches the stable solution.

The injection-locking bandwidth of the grid is a function of the incident angle of the injected signal. It is maximum for

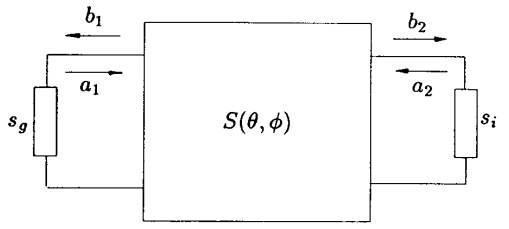

Fig. 17. Equivalent circuit for the grid as a receiver and transmitter. The radiated wave from the grid is a_1, and the injected wave is b_1. The wave a_2 feeds the horn (Fig. 11), and b_2 is the wave received from the grid. The scattering matrix $S(\theta,\phi)$ takes into account the grid pattern, the free-space attenuation, and the horn pattern.

normal incidence and decreases sharply as the angle varies from the normal (Fig. 16). The pattern is very similar to the transmitting field pattern, which is indicated on the same figure. It might seem surprising that the injection-locking bandwidth has the same pattern as the transmitting grid, but this is actually a consequence of reciprocity. We can understand this by considering a general equivalent circuit for an injection-locked grid, shown in Fig. 17. The grid reflection coefficient is s_g, and the source of the injection signal has a reflection coefficient s_i. The scattering matrix $S(\theta,\phi)$ takes into account the grid pattern, the free-space attenuation, and the horn pattern. It is linear and reciprocal, and we assume it to be matched. The radiated wave from the grid a_1 produces a wave b_2 in the far field. A wave a_2, which feeds the horn from the injection source, produces the injected wave b_1 at the grid, so we have

$$b_1 = s_{12}a_2 \tag{8}$$

$$b_2 = s_{21}a_1 \tag{9}$$

where $s_{21}(\theta,\phi)$ is effectively the transmitting grid pattern and $s_{12}(\theta,\phi)$ is effectively a receiving pattern. By reciprocity, these must be equal. From Fig. 12, the injection-locking bandwidth is proportional to the injected field magnitude $|b_1|$, which is in turn proportional to $s_{12}(\theta,\phi)$ and to the transmitted wave $|b_2|$. Fig. 16 confirms this interesting result.

V. Conclusion

A 100-MESFET oscillator is demonstrated. The oscillator is planar and suitable for monolithic integration. All the devices share the same biasing and tuning circuit, which makes this structure attractive for combining a very large number of solid-state devices on a single wafer. At higher frequencies, the wafer diameter measured in wavelengths increases, so the directivity should increase. In addition, the period of the grid is a fixed fraction of a wavelength, so the number of devices increases as well. For example, at 90 GHz, with a grid period of 0.5 mm ($\lambda/6$), a 50-mm GaAs wafer is 16 wavelengths across and would have 7500 devices. The grid should have a directivity of 30 dB and an ERP of 16 kW, assuming each device can produce 2 mW. The grid oscillator has the potential to overcome the limited power of individual solid-state millimeter-wave devices.

References

[1] J. W. Mink, "Quasi-optical power combining of solid-state millimeter-wave sources," *IEEE Trans. Microwave Theory Tech.*, vol. MTT-34, pp. 273–279, Feb. 1986.

[2] Z. B. Popović, M. Kim, and D. B. Rutledge, "Grid oscillators," *Int. J. Infrared and Millimeter Waves*, vol. 9, no. 7, pp. 647–654, July 1988.

[3] Z. B. Popović, R. M. Weikle, M. Kim, K. A. Potter, and D. B. Rutledge, "Bar-grid oscillators," *IEEE Trans. Microwave Theory Tech.*, vol. 38, pp. 225–230, Mar. 1990.

[4] R. A. York and R. C. Compton, "A 4 by 4 active array using Gunn-diodes," in *IEEE Int. APS Conf. Dig.* (Dallas, TX), June 1990, pp. 1146–1149.

[5] M. Kao *et al.*, "Very high power-added efficiency and low-noise 0.15-μm gate-length pseudomorphic HEMT's," *IEEE Electron Device Lett.*, vol. 10, pp. 580–582, Dec. 1989.

[6] P. M. Asbeck *et al.*, "Heterojunction bipolar transistors for microwave and millimeter-wave integrated circuits," *IEEE Trans. Microwave Theory Tech.*, vol. MTT-35, pp. 1462–1470, Dec. 1987.

[7] E. R. Brown, T. C. L. G. Sollner, C. D. Parker, W. D. Goodhue, and C. L. Chen, "Oscillations up to 420 GHz in GaAs/AlAs resonant tunneling diodes," *Appl. Phys. Lett.*, vol. 55, no. 17, pp. 1777–1779, Oct. 1989.

[8] C. Stephan and T. Itoh, "Planar quasi-optical subharmonically pumped mixer characterized by isotropic conversion loss," *IEEE Trans. Microwave Theory Tech.*, vol. MTT-32, pp. 97–102, Jan. 1984.

[9] R. F. Harrington, *Time-Harmonic Electromagnetic Fields*. New York: McGraw-Hill, 1961, p. 349.

[10] R. L. Eisenhart and P. J. Kahn, "Theoretical and experimental analysis of a waveguide mounting structure," *IEEE Trans. Microwave Theory Tech.*, vol. MTT-19, pp. 706–719, Aug. 1971.

[11] D. B. Rutledge, D. P. Neikerk, and D. P. Kasilingam, "Integrated circuit antennas," *Infrared and Millimeter-Waves*, vol. 10, pp. 1–87, 1983.

[12] K. Kurokawa, "Injection-locking of microwave solid-state oscillators," *Proc. IEEE*, vol. 61,. pp. 1386–1410, Oct. 1973.

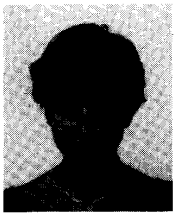

Zoya B. Popović was born in Belgrade, Yugoslavia, in 1962. She received the Dipl. Ing. degree from the University of Belgrade in 1985, and the M.S. and Ph.D. degrees from the California Institute of Technology, Pasadena, in 1986 and 1990, respectively.

In August 1990, she joined the faculty at the University of Colorado at Boulder as an Assistant Professor in Electrical Engineering. Her research interests include millimeter-wave quasi-optical techniques, microwave and millimeter-wave active antennas, nonlinear solid-state microwave device characterization, and microwave modulation of optical signals.

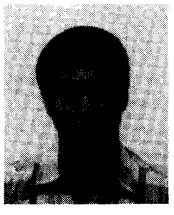

Robert M. Weikle II was born in Tacoma, WA, on February 13, 1963. He received the B.S. degree in electrical engineering and physics from Rice University, Houston, TX, in 1986 and the M.S. degree in electrical engineering from the California Institute of Technology in 1987. His research interests include high-frequency solid-state devices and millimeter-wave quasi-optical techniques. Currently he is working toward the Ph.D. degree at Caltech.

Mr. Weikle is a member of Phi Beta Kappa, Tau Beta Pi, and the American Physical Society.

✠

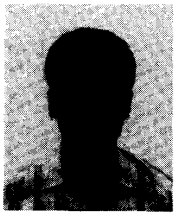

Moonil Kim was born in Seoul, Korea, on March 14, 1965. He received the B.S. degree from Illinois Institute of Technology in 1987 and the M.S. degree from the California Institute of Technology in 1988. He is currently working toward the Ph.D. degree as a member of the MMIC group at Caltech. He has been working on millimeter-wave power combining and beam steering circuitry.

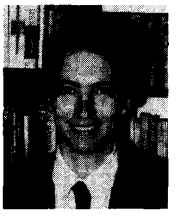

David B. Rutledge (S'75–M'80–SM'89) was born in Savannah, GA, on January 12, 1952. He received the B.A. degree in mathematics from Williams College, Williamstown, MA, in 1973, the M.A. degree in electrical sciences from Cambridge University, Cambridge, England, in 1975, and the Ph.D. degree in electrical engineering from the University of California at Berkeley in 1980.

In 1980 he joined the faculty at the California Institute of Technology, Pasadena, where he is now Professor of Electrical Engineering. His research is in developing millimeter- and submillimeter-wave monolithic integrated circuits and applications, and in software for computer-aided design and measurement. He is coauthor of the software CAD program *Puff*, which has over 6000 users worldwide.